Interface modes for monolithic nonlinear photonics

Arghavan Arjmand, Payam Abolghasem, Junbo Han, and Amr S. Helmy*

The Edward S. Rogers Sr. Department of Electrical and Computer Engineering and the Institute of Optical Sciences, University of Toronto, Toronto, Ontario M5S 3G4, Canada
**Corresponding author: a.helmy@utoronto.ca*

Received November 28, 2014; revised January 22, 2015; accepted January 22, 2015; posted January 22, 2015 (Doc. ID 228725); published March 11, 2015

A design methodology for obtaining versatile interface modes in monolithic structures is discussed. These modes are then utilized in conjunction with total internal reflection modes for phase-matching second-harmonic generation (SHG) in periodic layered media in Al_xGa_{1-x} As material system. Typical loss values of 2.71 cm^{-1} for a TE-polarized pump and 4.26 cm^{-1} for a TM-polarized pump around 1550 nm were obtained. Nonlinear characterizations are carried out using 2 ps, 30 ps, and a continuous wave pump for type-I and type-II interactions. Maximum SHG conversion efficiency of $1.14 \times 10^4\%$ W^{-1} cm^{-2} is observed for the type-II process with a pump power of 0.52 mW in a sample with a length of 2.0 mm.

OCIS codes: (190.4410) Nonlinear optics, parametric processes; (130.7405) Wavelength conversion devices; (060.3735) Fiber Bragg gratings; (190.4390) Nonlinear optics, integrated optics.
http://dx.doi.org/10.1364/JOSAB.32.000577

1. INTRODUCTION

Efficient second-order nonlinear processes in compound semiconductors, particularly GaAs/Al_xGa_{1-x}As, have been studied utilizing different phase-matching (PM) techniques. Methods such as form birefringence [1], high-Q resonant cavities [2] and quasi-phase matching [3] have been implemented to achieve PM in different material systems. Despite their capability to demonstrate tabletop optical parametric oscillation [4], these methods fail to allow for monolithic integration of frequency conversion elements and active devices, including diode laser pumps, photodetectors, and semiconductor amplifiers. Recent studies have demonstrated a PM technique enabled by Bragg reflection waveguides (BRWs) [5]. In BRWs, PM is achieved between the interacting modes guided by different mechanisms, namely, total internal reflection (TIR) and transverse Bragg reflection (TBR). BRW PM is particularly attractive as a robust platform for the monolithic integration of low-loss passive and active elements [6]. This technique has demonstrated various χ^2 processes such as second-harmonic generation (SHG), difference (DFG), and sum frequency generation (SFG) in monolithic waveguides [7–9], entangled photon generation [10], and optical parametric generation in laser diodes [11].

While BRWs have provided a novel route for PM χ^2 nonlinearities in semiconductors, the method is associated with some limitations and can benefit from further optimization. For instance, in conventional quarter-wave BRWs (QtW-BRWs), the core thickness is restricted to a few hundreds of nanometers, resulting in a poor confinement factor combined with a degraded spatial overlap factor between the modes of the interacting waves and challenges in the light in-coupling efficiency. Moreover, in quantum optical applications, where entangled photons are generated through spontaneous parametric downconversion, the state of the entangled photons resulting from this process and the quality of entanglement can be engineered through control of properties of the three interacting waves, namely, the pump, signal, and idler. One of the most powerful means of exercising control over the pump, signal, and idler is to have them propagate in three separate modes. This can provide a superior level of control over their properties, including dispersion and birefringence, among others [10,12]. Having TIR and BRW modes coexisting with another type of mode in the same structure can enable this control.

D'yakonov waves belong to one type of interface modes (IMs), which was predicted theoretically in 1988 [13] and demonstrated experimentally by Takayama *et al.* [14]. D'yakonov waves occur at the boundary between two transparent media and can take place in several configurations involving an isotropic material and a uniaxial or biaxial homogeneous medium, under positive birefringence conditions. Combinations of materials with such stringent requirements are poorly suited to monolithic integration and require stringent structural parameter tolerance to meet the D'yakonov wave criteria [15]. Tamm modes are also IMs that are supported by structurally chiral materials, relaxing the homogeneity condition in the direction normal to the interface [16]. Both D'yakonov waves and Tamm modes have potential applications in sensing as well as waveguiding. However, due to their restrictive material requirements, their monolithic integration with other devices is challenging. Bloch IMs are another type of IMs that exist at the boundary of a homogenous medium and a periodic layered medium, as shown in Fig. 1(a), or two periodic layered media, as illustrated in Fig. 1(b) [17]. As seen in these figures, the same structures that accommodate propagation of the TIR modes and Bragg modes discussed, for example, in [18] can also support optical modes that exist at the interface between the periodic cladding and the core. These are based on IMs, which we previously reported [19]. Interface mode waveguides (IMWs) could be utilized in a similar fashion to what has been carried out in the past utilizing BRWs to facilitate efficient three-wave mixing and to provide an additional

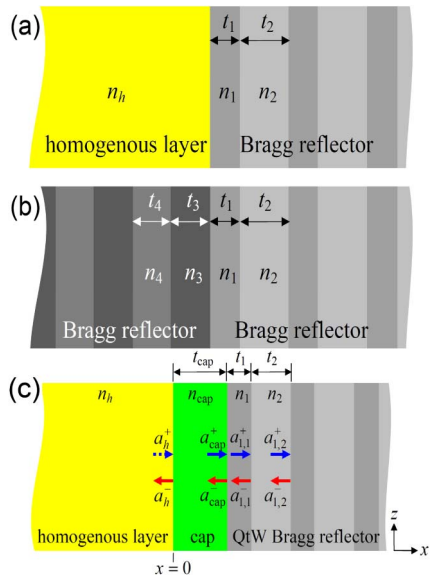

Fig. 1. Schematics of three types of interface modes between (a) a homogenous dielectric layer and a Bragg stack; (b) two different Bragg stacks; (c) a homogenous layer separated from the Bragg stack by a cap layer to enable tuning of mode attributes.

degree of freedom for alleviating the limitations associated with conventional BRWs when used in PM applications.

In this paper, a new class of modes and the design methodology associated with obtaining this versatile class of IMs in monolithic structures are discussed. Phase-matching second-order nonlinearity in these structures is then elucidated. After, the observation of a second-order nonlinear interaction employing this new class of IMs, in the $Al_xGa_{1-x}As$ material system, is demonstrated. SHG is used here to demonstrate the potential of IMs in three-wave mixing processes. Nevertheless, the technique can be utilized for other three-wave mixing processes, including SHG and DFG.

2. BLOCH INTERFACE MODES

The modal properties of Bloch IMs in multilayer media will first be reviewed, and their potential for integrated photonics applications will then be discussed. The simplest cases of electromagnetic Bloch surface modes take place at the interface of a semi-infinite periodic layered medium and a homogenous medium and also at the interface of two semi-infinite periodic layered media, which can be seen in Figs. 1(a) and 1(b), respectively [17]. In the figures, the periodic stack is composed of dielectric layers with material indices n_1 and n_2 and associated thicknesses of t_1 and t_2 with periodicity $\Lambda = t_1 + t_2$. The semi-infinite homogenous layer has an index of n_h. It is assumed that propagation is in the $+z$ direction in which the general solution of the wave equation is

$$\psi(x,z,t) = \psi(x)\exp[i(\omega t - \beta z)], \tag{1}$$

where ω is the angular frequency, $\beta = k_0 n_{\text{eff}}$ is the propagation constant, k_0 is the wavenumber in free space, n_{eff} is the effective mode index, and $\psi(x)$ is the field envelope in the transverse direction, along the x axis. For TE polarization, the nonzero field components are (H_x, E_y, H_z) with $\psi(x) = E_y$. For TM polarization, the field components are (E_x, H_y, E_z) with $\psi(x) = H_y$ [17].

Another variation of IMs can occur at the boundary of semi-infinite periodic media with a high refractive index cap layer and a homogeneous medium. Such a structure is capable of guiding TIR modes as well as IMs [19]. A schematic of such structure is shown in Fig. 1(c), where the cap layer is assumed to have a refractive index of n_{cap} with a thickness of t_{cap}. The field equations inside the layers of this structure can be written as

$$\psi_y(x) = \begin{cases} a_h^- \exp(q_h^x x) \\ x < 0 \\ a_{\text{cap}}^+ \exp[-ik_{\text{cap}}^x (x - t_{\text{cap}})] \\ + a_{\text{cap}}^- \exp[+ik_{\text{cap}}^x (x - t_{\text{cap}})] \\ 0 \le x \le t_{\text{cap}} \\ a_{j,1}^+ \exp[-ik_1^x (x - j\Delta_{j,1})] \\ + a_{j,1}^- \exp[+ik_1^x (x - j\Delta_{j,1})] \\ t_{\text{cap}} + (j-1)\Lambda \le x \le t_{\text{cap}} + j\Lambda - t_2 \\ a_{j,2}^+ \exp[-ik_2^x (x - j\Delta_{j,2})] \\ + a_{j,2}^- \exp[+ik_2^x (x - j\Delta_{j,2})] \\ t_{\text{cap}} + j\Lambda - t_2 \le x \le t_{\text{cap}} + j\Lambda \end{cases}, \tag{2}$$

where $\Delta_{j,1} = t_{\text{cap}} + j\Lambda - t_2$, $\Delta_{j,2} = t_{\text{cap}} + j\Lambda$ $(j = 1, 2, \ldots)$, and a_{cap}^+ and a_{cap}^- are the field amplitudes of the right and left traveling waves in the cap layer. For the modes discussed here, the field inside the homogenous layer with refractive index n_h is evanescent. As such, the right propagating field amplitude within the homogenous layer vanishes, $a_h^+ = 0$. Moreover, the magnitude of the left propagating field amplitude within the homogenous layer can be considered as unity: $a_0^- = 1$. Using the transfer matrix method, one can relate the field amplitudes of the cap layer, a_{cap}^+ and a_{cap}^-, to obtain

$$a_{\text{cap}}^+ = \frac{1}{2}(1 - f_{\text{cap}})\exp(-i\phi_{\text{cap}}), \tag{3a}$$

$$a_{\text{cap}}^- = \frac{1}{2}(1 + f_{\text{cap}})\exp(+i\phi_{\text{cap}}), \tag{3b}$$

where $\phi_{\text{cap}} = k_{\text{cap}}^x t_{\text{cap}}$ is the accumulated phase within the cap layer and

$$f_{\text{cap}} = \begin{cases} \frac{iq_h^x}{k_{\text{cap}}^x} & \text{for TE polarization} \\ \frac{n_{\text{cap}}^2 q_h^x}{n_c^2 k_{\text{cap}}^x} & \text{for TM polarization} \end{cases}. \tag{4}$$

Utilizing the cap layer between the homogenous medium and the Bragg stack as a design parameter allows one to tailor the accumulated phase in the layer with index n_h. This can then be used to render the effect of the periodic stack to resemble that of a QtW stack. In this case,

$$\begin{aligned} k_1^x t_1 &= (2u+1)\pi/2 \\ k_2^x t_2 &= (2v+1)\pi/2, \end{aligned} \tag{5}$$

where $u, v = 0, 1, 2, \ldots$. Imposing the constraint of QtW offers the advantage of maximizing the evanescent field decay rate within the stack. In addition, this allows for analysis of this structure to proceed using analytical formalism, while assuming that QtW Bragg mirrors are utilized irrespective of the stack dimensions. The modes for a representative example for a structure similar to the schematic described in Fig. 1(c) using a QtW periodic stack are shown in Fig. 2. Using the QtW periodic stack offers the remarkable feature of pinning the

field at the boundary of the cap layer and the Bragg reflector at $x = t_{cap}$, so that it is allowed to either vanish (node) or peak (antinode). In the former case, the Bragg reflector acts as a perfect electric wall, where the tangential component of the electric field vanishes at the interface between the cap layer and the periodic stack. In this case, the amplitudes of the right and left propagating plane waves inside the cap layer should cancel out such that $a^{+}_{cap} + a^{-}_{cap} = 0$. In contrast, the latter case resembles a perfect magnetic wall, where the first-order derivative of the electric field vanishes at $x = 0$ dictating that $a^{+}_{cap} - a^{-}_{cap} = 0$. Using this behavior for the case of a QtW stack and employing the field amplitudes in 3, one can readily derive the dispersion relation of TE propagating IM in the structure of Fig. 1(c) as

$$\cot(k^{x}_{cap} t_{cap}) = +\frac{q^{x}_{h}}{k^{x}_{cap}} \qquad (k^{x}_{cap} \le (k^{x}_{1})), \tag{6a}$$

$$\tan(k^{x}_{cap} t_{cap}) = -\frac{q^{x}_{h}}{k^{x}_{cap}} \qquad (k^{x}_{cap} > k^{x}_{1}). \tag{6b}$$

Similarly, for TM polarization, modal dispersion can be written as

$$\cot(k^{x}_{cap} t_{cap}) = +\frac{n^{2}_{cap} q^{x}_{h}}{n^{2}_{h} k^{x}_{cap}} \qquad (n^{2}_{h} k^{x}_{cap} < n^{2}_{cap} k^{x}_{1}), \tag{7a}$$

$$\tan(k^{x}_{cap} t_{cap}) = -\frac{n^{2}_{cap} q^{x}_{h}}{n^{2}_{h} k^{x}_{cap}} \qquad (n^{2}_{h} k^{x}_{cap} > n^{2}_{cap} k^{x}_{1}). \tag{7b}$$

The dispersion relations of the example structure shown in Fig. 2 are plotted in Figs. 3(a) and 3(b), for TE and TM polarization, respectively. The dispersion diagrams show shaded regions where the states of the Bragg stack reside. The gaps within these regions represent bandgaps in the optical states, where no modes take place for the stack parameters used. In these diagrams, there exists also the light lines for the materials with the largest and smallest refractive indices within the structure. Those correspond to the cap and homogenous (core) layer refractive indices, respectively. It can be seen from the figures that interface and TIR modes are present. The TIR modes exist outside of bandgap region of the stack, while the IMs reside within the photonic bandgap of the stack. The TIR modes are not bound by the multilayer periodicity and, hence, reside above the light line of the cap layer (highest index layer) and below the light line of the homogenous core layer (smallest index layer). These modes are guided in the cap layer, as they have an oscillatory field in the cap and evanescent field in the homogenous core. The IM mode are Bloch IMs guided by the multilayer periodicity. Their indices reside above the light line of the cap layer, corroborating that this mode exhibits an evanescent field in the core region in agreement with the field distributions in Fig. 2. There is a set of two modes for the TE and TM polarizations: the zero- and first-order modes for the parameters of this structure.

It is useful to note that the IMs at the boundary of a homogenous medium and a multilayer stack are also referred to as surface modes and have been used in numerous applications to date [16]. However, the design alternative that employs the cap layer discussed here benefits from an additional degree of freedom in device design. It has been shown that the cap layer of a periodic multilayer stack affects the position of surface modes within the band structure [20], hence controlling the dispersion properties of the modes. Studies have already taken advantage of this cap layer for more sensitive and more flexible sensors [21–23].

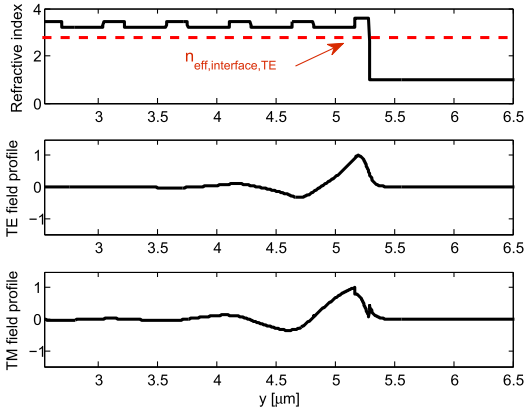

Fig. 2. TE and TM mode profiles for interface modes at the boundary between a semi-infinite periodic Bragg stack with a cap layer and a homogeneous medium; the index profile is also shown in the top plot. The dashed line indicates the TE mode effective index.

A. Interface Mode Waveguides

An IMW can be designed by bringing together two identical IM structures, as shown in Fig. 4. This results in a symmetric structure that supports the propagation of two IMs, which,

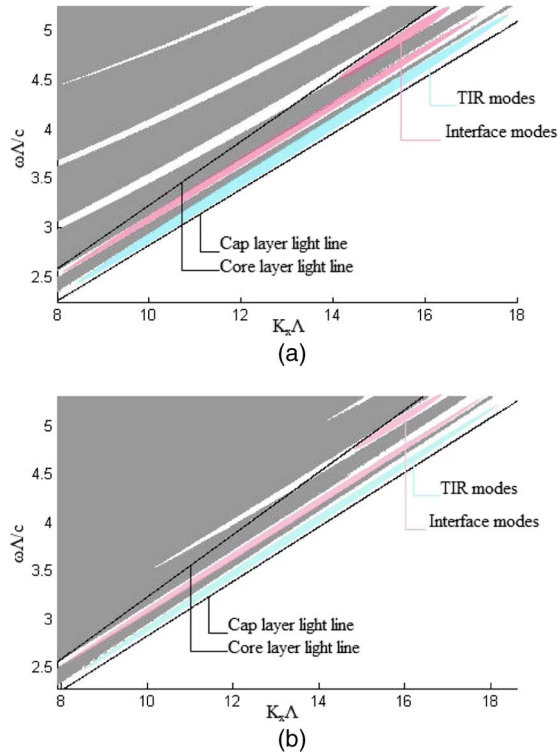

Fig. 3. (a) TE and (b) TM band diagrams at the boundary between a semi-infinite periodic layered medium with a cap layer and a homogeneous medium. n_L = largest refractive index; n_S = smallest refractive index. The guided modes are indicated on the plots.

when brought in close proximity of one another, can couple. These modes take place at the interfaces between the cap layers and left- and right-hand QtW stacks. In this design, which will be referred to as IMW, the homogenous medium plays the role of the waveguide core. In contrast to conventional TIR waveguides, the modal field in this class of waveguides is evanescent in the core.

The amplitudes of the right and left propagating plane waves within the core of the structure shown in Fig. 4, a_h^+ and a_h^-, are defined at the waveguide center at $x = 0$. Due to the symmetry of the structure studied here and without loss of generality, one can assume that $a_h^+ = a_h^- = 1/2$ or $a_h^+ = -a_h^- = 1/2$. The former case deals with even modes, while the latter is related to modes with odd spatial symmetry. Here, we focus on analyzing even modes, as we are most interested in the fundamental mode of the structure. However, the analysis can be easily extended to odd modes. Using the transfer matrix method, one can relate $a_h^+ = a_h^-$ to $a_{\text{cap}}^+ = a_{\text{cap}}^-$ to obtain

$$a_{\text{cap}}^+ = \frac{1}{2}\exp(-ik_{\text{cap}}^x t_{\text{cap}}) - \frac{1}{2}\frac{q_c^x}{k_{\text{cap}}^x}\exp(-ik_{\text{cap}}^x t_{\text{cap}}), \tag{8a}$$

$$a_{\text{cap}}^- = \frac{1}{2}\exp(+ik_{\text{cap}}^x t_{\text{cap}}) + \frac{1}{2}\frac{q_c^x}{k_{\text{cap}}^x}\exp(+ik_{\text{cap}}^x t_{\text{cap}}), \tag{8b}$$

where $q_c^x = k_0\sqrt{n_{\text{eff}}^2 - n_c^2}$ is the real-valued wave vector within the core. Applying the boundary conditions at the interface of the cap layer with QtW Bragg reflectors yields the modal dispersion of IMWs. For TE polarization, the modal dispersion can be expressed as

$$\coth(q_c^x t_c/2)\cot(k_{\text{cap}}^x t_{\text{cap}}) = +\frac{q_c^x}{k_{\text{cap}}^x} \qquad (k_{\text{cap}}^x < k_1^x), \tag{9a}$$

$$\coth(q_c^x t_c/2)\tan(k_{\text{cap}}^x t_{\text{cap}}) = -\frac{q_c^x}{k_{\text{cap}}^x} \qquad (k_{\text{cap}}^x > k_1^x). \tag{9b}$$

Similarly, for TM polarization, the dispersion relation can be expressed as

$$\coth(q_c^x t_c/2)\cot(k_{\text{cap}}^x t_{\text{cap}}) = +\frac{n_{\text{cap}}^2 q_c^x}{n_c^2 k_{\text{cap}}^x} \qquad (n_1^2 k_{\text{cap}}^x < n_{\text{cap}}^2 k_1^x), \tag{10a}$$

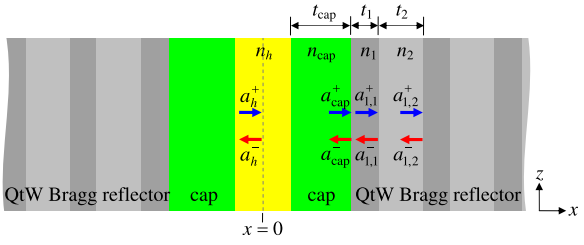

Fig. 4. A schematic of a coupled interface mode waveguide composed of a homogenous layer separated on either side by cap layers then quarter-wave Bragg reflectors.

$$\coth(q_c^x t_c/2)\tan(k_{\text{cap}}^x t_{\text{cap}}) = -\frac{n_{\text{cap}}^2 q_c^x}{n_c^2 k_{\text{cap}}^x} \qquad (n_1^2 k_{\text{cap}}^x > n_{\text{cap}}^2 k_1^x). \tag{10b}$$

Equation (9) can be solved to determine the required thickness of the cap layer, which guarantees that the bilayers of the Bragg stacks are QtW thick. As such, for TE polarization, t_{cap} can be derived as

$$t_{\text{cap}} = \frac{1}{k_{\text{cap}}^x}\left[\operatorname{acot}\left(+\frac{q_c^x}{k_{\text{cap}}^x}\zeta\right) + p\pi\right] \qquad (k_{\text{cap}}^x < k_1^x), \tag{11a}$$

$$t_{\text{cap}} = \frac{1}{k_{\text{cap}}^x}\left[\operatorname{atan}\left(-\frac{q_c^x}{k_{\text{cap}}^x}\zeta\right) + p\pi\right] \qquad (k_{\text{cap}}^x > k_1^x), \tag{11b}$$

where $p = 0, 1, 2, \ldots$ is the scaling factor of the cap layer thickness, which can take various values, and ζ is a real valued parameter defined as

$$\zeta = \tanh(q_c^x t_c/2). \tag{12}$$

Using Eq. (10), for TM polarization the cap layer thickness is calculated according to

$$t_{\text{cap}} = \frac{1}{k_{\text{cap}}^x}\left[\operatorname{acot}\left(+\frac{n_{\text{cap}}^2 q_c^x}{n_c^2 k_{\text{cap}}^x}\zeta\right) + p\pi\right] \qquad (n_1^2 k_{\text{cap}}^x < n_{\text{cap}}^2 k_1^x), \tag{13a}$$

$$t_{\text{cap}} = \frac{1}{k_{\text{cap}}^x}\left[\operatorname{atan}\left(-\frac{n_{\text{cap}}^2 q_c^x}{n_c^2 k_{\text{cap}}^x}\zeta\right) + p\pi\right] \qquad (n_1^2 k_{\text{cap}}^x > n_{\text{cap}}^2 k_1^x). \tag{13b}$$

The modes for a representative example of a structure similar to the schematic described in Fig. 4 using a QtW periodic stack are shown in Fig. 5. The resemblance to the fields observed in single-sided examples given in Fig. 2 is evident; however, now the core region is bound by a Bragg stack from either side. In the cases where the core size is smaller than the wavelength of operation, the IMs on either side of the core couple strongly. This eliminates the odd modes, and only the even modes take place in such structures. Eliminating the odd modes assists with fundamental mode discrimination, which is useful in using these structures as the core for a single transverse mode in diode lasers [6]. The figure also shows the field distribution of the TIR mode, which exists alongside the IMs in this structure. The effective index of the IM and the TIR modes are shown in red and blue dashed lines, respectively, superimposed on the index profile of the structure.

The band structures of both polarizations are plotted in Fig. 6. TIR and IMs coexist in this structure. The TIR modes are not bound by the multilayer periodicity and, hence, reside above the light line of the cap layer (highest index layer) and below the light line of the homogenous core layer (smallest index layer. These modes are guided in the cap layer, as they have an oscillatory field in the cap and evanescent field in the homogenous core. This structure supports only a zero-order IM in both polarizations. The IM modes are guided by the multilayer periodicity; hence, their indices reside above the light line of the cap layer, corroborating that this mode exhibits an

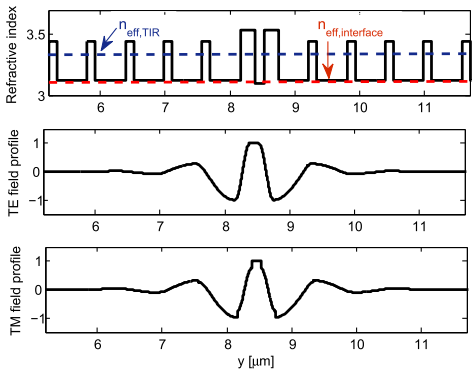

Fig. 5. TE and TM mode profiles of an interface mode at the boundary between two semi-infinite periodic layered media with cap layers separated by a thin homogenous medium layer. Red and blue dashed lines on the plot of the index profile designate interface mode and TIR mode effective indices, respectively.

evanescent field in the core region in agreement with the field distributions in Fig. 5.

The dispersion of IMWs is similar to those of Bragg modes investigated in [24]. The main difference arises from the fact that the range for the IM effective index values is different from that of Bragg modes. In BRWs, the field is nonevanescent within the core as well as the cladding. This constrains the range of the effective mode index to

$$0 < n_{\mathrm{eff,BRW}} < n_{\mathrm{min}}, \tag{14}$$

where n_{min} is the minimum refractive index of the structure, including the core and bilayers of the Bragg mirrors. However, for the coupled IM studied here, the field is evanescent in the core; hence, the mode effective index is limited by the core refractive index as

$$n_c < n_{\mathrm{eff,IM}} < n_{\mathrm{min}}. \tag{15}$$

In much the same way that the modes in BRW with a cap between the Bragg stacks and the core provided more tuning parameters and, hence, more flexible design capabilities than those in BRW without a cap [24], IMW using the capped periodic media offers greater degrees of freedom over their conventional noncapped counterpart. This can enable better control over group velocity dispersion (GVD) and group velocity mismatch (GVM) for ultrafast pulse propagation applications. However, they can offer this control using structures that exhibit significantly lower optical losses in comparison to approaches that provide dispersion engineering utilizing 2D photonic bandgap waveguides [25,26].

3. PHASE-MATCHING INTERFACE MODE WAVEGUIDES

Efficient three-wave mixing processes require the PM condition between the interacting waves to be maintained. For SHG devices in $Al_xGa_{1-x}As$, which will be the material of choice in this work, two processes, namely, type-I and type-II, can be phase-matched. In type-I PM, the k vector of the TE-polarized pump is matched to that of the TM-polarized second-harmonic wave. In type-II PM, the k vectors of a pump mode with hybrid TE + TM polarization states are matched to a second harmonic with TE polarization state. The PM conditions of these two scenarios are expressed as

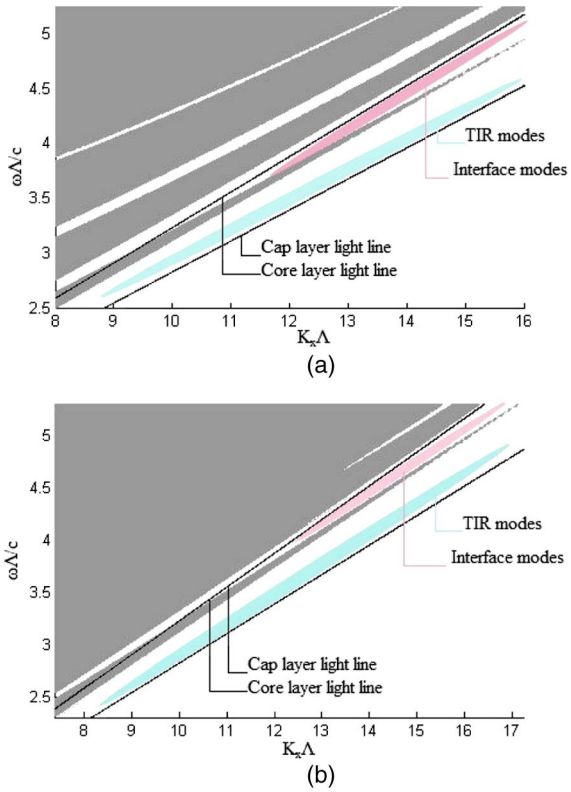

Fig. 6. (a) TE and (b) TM band diagrams at the boundary between two semi-infinite periodic layered media with cap layers separated by a thin homogenous layer. The guided modes are indicated on the plots.

$$\text{Type-I: } n_{\mathrm{eff},2\omega}^{(\mathrm{TM})} = n_{\mathrm{eff},\omega}^{(\mathrm{TE})}, \tag{16a}$$

$$\text{Type-II: } n_{\mathrm{eff},2\omega}^{(\mathrm{TE})} = 0.5[n_{\mathrm{eff},\omega}^{(\mathrm{TE})} + n_{\mathrm{eff},\omega}^{(\mathrm{TM})}], \tag{16b}$$

where $n_{\mathrm{eff},\omega}^{(\mathrm{TE})}$ and $n_{\mathrm{eff},\omega}^{(\mathrm{TM})}$ are the effective mode indices of fundamental TE- and TM-polarized pump modes, respectively, and $n_{\mathrm{eff},2\omega}^{(\mathrm{TE})}$ and $n_{\mathrm{eff},2\omega}^{(\mathrm{TM})}$ are those of the second-harmonic (SH) signal. As a case study, consider the type-II SHG of a pump (ω) at 1550 nm, which generates a second-harmonic (2ω) at 775 nm. Figures 7(a) and 7(b) illustrate the index profiles of the structure at the pump and second-harmonic wavelengths. The dashed lines in the two figures denote the effective mode indices for a structure where PM is achieved. The structure consists of a core layer, followed by a cap layer on either side followed by Bragg reflectors satisfying the QtW condition for the pump wavelength. The field profiles of the TE- and TM-polarized pump modes and TE-polarized SH are shown in Figs. 7(c) and 7(d), respectively. Two types of modes with different types of confinement coexist at two different frequencies in the same structure. The device can be designed such that it accommodates fundamental modes of each type, TE and TM polarized, which are guided via TIR at the pump wavelength and a TE-polarized coupled IM at the SH wavelength.

In the calculations of the structure properties, the TIR modes can be studied using the same equations employed for the calculation of the IMW. In reality, the effective mode index of TIR modes resides somewhere between the core index and the cladding indices and is, hence, confined within

the two caps and core layers through TIR. Using the design methodology in [19], given the core thickness, the structure refractive indices, and the thickness of the cap, the thicknesses of the bilayers composing the periodic cladding can be determined for the QtW condition. The following procedure describes the route used for designing phase-matched waveguides that utilize IMs for SH generation:

1. Define and discretize the range of effective mode indices, $N_{\mathrm{eff},2\omega} \in (n_{\mathrm{core},2\omega}, n_{\mathrm{min},2\omega})$ where $n_{\mathrm{min},2\omega}$ denotes the smallest refractive index within the structure at second-harmonic wavelength.
2. For each mode index $n_{\mathrm{eff},2\omega} \in N_{\mathrm{eff},2\omega}$, calculate the transverse wave vector, $k_j^x, j \in \{1, 2, \mathrm{cap}\}$, according to $k_j^x = k_0\sqrt{n_j^2 - n_{\mathrm{eff},2\omega}^2}$, where k_0 is the wave vector in free space.
3. Using the QtW condition of $k_1^x t_1 = k_2^x t_2 = \pi/2$, obtain the thicknesses of the bilayers of the Bragg reflectors.
4. Use the dispersion relations in [19] to calculate the corresponding cap layer thickness for both TE and TM IMs.
5. With the index and thickness values obtained, calculate the effective mode indices of the TE- and TM-polarized TIR modes at pump wavelength.
6. Use the PM conditions in Eq. (16) to determine the phase-matched structure parameters.

4. WAVEGUIDE OPTIMIZATION FOR ENHANCED NONLINEAR INTERACTION

Several process parameters can be tailored in order to maximize second-order nonlinear conversion. The most important parameter is the nonlinear coupling efficiency, ξ. This parameter defines how effectively energy is coupled between the pump and SH modes. By definition, the nonlinear coupling efficiency for a phase-matched SHG process can be defined as [27]

$$\xi = \frac{1}{n_{\mathrm{eff}}^3 t_{\mathrm{SHG}}^{\mathrm{eff}}} = \frac{1}{n_{\mathrm{eff}}^3}\frac{\left[\int_{-\infty}^{\infty}[E_{2\omega}(x)]^* \mathrm{d}(x)[E_{\omega}(x)]^2 \mathrm{d}x\right]^2}{\left[\int_{-\infty}^{\infty}[E_{\omega}(x)]^2 \mathrm{d}x\right]^2\left[\int_{-\infty}^{\infty}[E_{2\omega}(x)]^2 \mathrm{d}x\right]}, \tag{17}$$

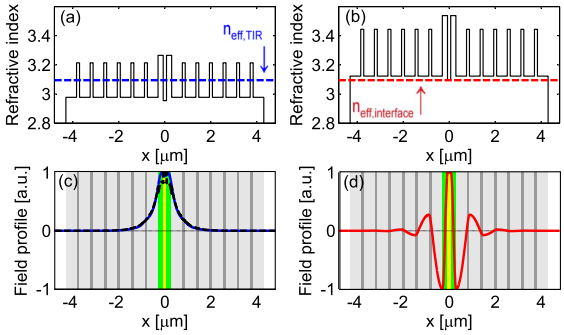

Fig. 7. The index profile of a representative coupled interface mode waveguide (a) at the pump wavelength of 1550 nm and (b) at the SH wavelength of 775 nm. The dashed line in (a) is the average of the effective mode indices of the fundamental TE and TM at the pump wavelength. The dashed line in (b) is the mode index of the TE at the SH wavelength. The field profiles shown are those of the (c) TE pump (solid line), TM pump (dashed line), and the (d) TE SH mode.

where $t_{\mathrm{SHG}}^{\mathrm{eff}}$ is the effective SH width, n_{eff} is the effective mode index, and $d(x)$ denotes the spatial dependence of bulk effective second-order nonlinear coefficient of the layers. The calculation of $d(x)$ is based on a work by Ohashi *et al.* [28], in which reflected SH was used to experimentally determine the dependence of the magnitude of $d(x)$ on wavelength and the aluminum concentration in $\mathrm{Al}_x\mathrm{Ga}_{1-x}\mathrm{As}$.

A measurable parameter that is often used as a figure of merit to determine the efficiency of a SHG device is the normalized conversion efficiency, η_{norm}, defined as

$$\eta_{\mathrm{norm}} = \frac{P_{2\omega}}{P_{\omega}^2 L^2} = 2\omega^2 d_{\mathrm{eff}}^2 \xi \left(\frac{\mu_0}{\epsilon_0}\right)^{3/2}, \tag{18}$$

where P_ω and $P_{2\omega}$ are the internal pump and SH powers, respectively, L is the device length, d_{eff} is the structure effective nonlinear coefficient, and ϵ_0 and μ_0 are, respectively, the permittivity and permeability of free space. The device length also plays a role in the conversion efficiency. However, this effect is usually counteracted by the propagation losses in waveguides; hence, the normalized conversion efficiency, η_{norm}, is the widely adopted merit to gauge the performance of the SHG process.

In choosing the layer thicknesses and Al concentrations for a practical $\mathrm{Al}_x\mathrm{Ga}_{1-x}\mathrm{As}$ structure, several considerations are taken into account; the Al fraction in AlGaAs is limited in practice at the lower end to $x = 0.2$ due to increased two-photon absorption for smaller x factors [29]. It is also limited at the upper end to $x = 0.85$ to reduce the adverse effects of the rapid oxidization that takes place at high Al concentration. In what follows, the layer thicknesses and Al concentrations are referred to as t_i and x_i, where $i \in \{1, 2, \mathrm{cap}, \mathrm{core}\}$ for the first and second cladding layers adjacent to the cap layer, the cap layer, and the core layer, respectively.

The normalized conversion efficiency is studied as a function of x for all layers as well as the core thickness. The most dominant changes in the conversion efficiency lead to it, assuming its maximal value occurred in the parameter space of (t_{core}, x_2); therefore, η_{norm} was plotted as a function of these parameters. The contour plots of the normalized conversion efficiency as a function of the core thickness and the Al concentration of layer 2 with a refractive index n_2 layer for both type-I and type-II PM are provided in Figs. 8(a) and 8(b), respectively. From the figures, the normalized conversion efficiency for both PM schemes can be maximized over a practical range of core thicknesses in the region of 100 nm. The choice of parameter ranges was based on the capability of the structure to support phase-matched modes and the aforementioned design limitations.

From Fig. 8, it can be seen that, for a fixed value of the core thickness, the conversion efficiency increases as x_2 increases. This can be attributed to the increase in refractive index contrast between the cladding layers, n_1 and n_2, which further confines the SH mode. This higher refractive index contrast, in turn, gives rise to enhanced nonlinear coupling efficiency, ξ. However, for a fixed value of x_2, there exists a local maximum in the value of the conversion efficiency. For smaller core thickness values, the first negative lobes of the SH mode are significant, so that most of the wave energy is concentrated in these lobes, away from the three layers that constitute the core, where modal overlap between the pump and SH

is greatest. For larger core thicknesses, especially for lower x_2, the SH mode becomes less confined. The addition of side lobes, including those with the opposite sign to that of the TIR, is a factor that reduces the overlap between the two modes and, hence, the conversion efficiency. As such, there exists a point at which these two effects give rise to an optimum core thickness for a maximal attainable conversion efficiency for the range of parameters used in the design.

The temporal walk-off between the pump and SH in pulsed SHG is another significant parameter that plays an important role in increasing the nonlinear interaction and, hence, the process efficiency. GVM is a measure of this temporal walk-off. Minimizing GVM leads to more efficient nonlinear interaction between the interacting pulses in the case of pulsed pump. By definition, GVM is quantitatively expressed as

$$\mathrm{GVM} = \left|\frac{1}{v_{g,\omega}} - \frac{1}{v_{g,2\omega}}\right| = \frac{1}{c}|n_{g,\omega} - n_{g,2\omega}|, \tag{19}$$

where $n_{g,\omega}$ and $n_{g,2\omega}$ are the group indices of the pump and SH, respectively. A contour plot of the GVM as a function of (x_c, x_{cap}) for type-I PM is shown in Fig. 9. From the figure, the minimum GVM occurs at $(x_c, x_{\mathrm{cap}}) = (0.8, 0.35)$ with a value of 2.6354 ps/mm. For example, for using a 30 ps pulsed pump, the useful device length is limited to ≈1.1 cm before severe temporal walk-off between the pump and SH pulses takes place.

Another salient parameter, which is particularly relevant in ultrashort pulse applications, is the GVD. Apart from the undesirable pulse distortion that results from GVD, a reduction in the pulse peak power due to pulse broadening will further reduce nonlinear conversion efficiency. Minimizing GVD is, thus, essential for enhanced second-order interactions in cases of a femtosecond pump. By definition, the GVD at ω_σ angular frequency is given as

$$\mathrm{GVD}_{\omega_\sigma} = \frac{\partial^2 \beta_{\omega_\sigma}}{\partial \omega^2} = \frac{2}{c}\frac{\partial n_{\mathrm{eff},\omega_\sigma}}{\partial \omega} + \frac{\omega_\sigma}{c}\frac{\partial^2 n_{\mathrm{eff},\omega_\sigma}}{\partial \omega^2}, \tag{20}$$

where β_{ω_σ} is the propagation constant of the optical mode at ω_σ, and c is the speed of light in free space. Figures 10(a) and 10(b) illustrate the dependence of GVD on the Al concentrations of the core and cap layers obtained at the pump and SH frequencies, respectively. From the figures, it can be seen that the GVD of the SH propagating as a IMW mode is larger than that of the pump mode for the entire range of (x_c, x_{cap}). This larger GVD for the SH signal was expected, as the propagation of the IM relies on the resonance of the Bragg reflectors. Moreover, the material dispersion is larger at the SH wavelength.

It would be informative to compare nonlinear parameters of interest in the IMWs discussed here with those previously reported in phase-matched BRWs [18,24]. Tables 1, 2, and 3 provide a summary of such comparison obtained for type-I SHG in each device. In Table 1, each design aims at maximizing the normalized conversion efficiency. From the table, the maximum η_{norm} is obtained for the matching layer-based BRW (ML-BRW) design in [24], which was approximately an order of magnitude larger than those in conventional QtW-BRW and IMW. Contrary to the case of conventional QtW-BRWs [18], where there is a trade-off between η_{norm} and $\mathrm{GVD}_{2\omega}$ utilizing IMW modes benefits from the fact that enhanced conversion efficiency does not have to be at the cost of a greater GVD.

Table 2 compares the IMW design to the ML-BRW design in [24] where the GVM has been maximized. From the table, it can be deduced that, for similar GVM values, the design of ML-BRW benefits from larger conversion efficiency. Additionally, Table 3 draws a similar comparison where the SH GVD has been maximized. From the table, it can be seen that, for comparable $\mathrm{GVD}_{2\omega}$, conversion efficiency of the IMW device is superior to that of the ML-BRW design.

The optimization results discussed here indicate that the IMWs are capable of delivering efficiencies of the same order of magnitude as those obtained in conventional QtW-BRWs [18].

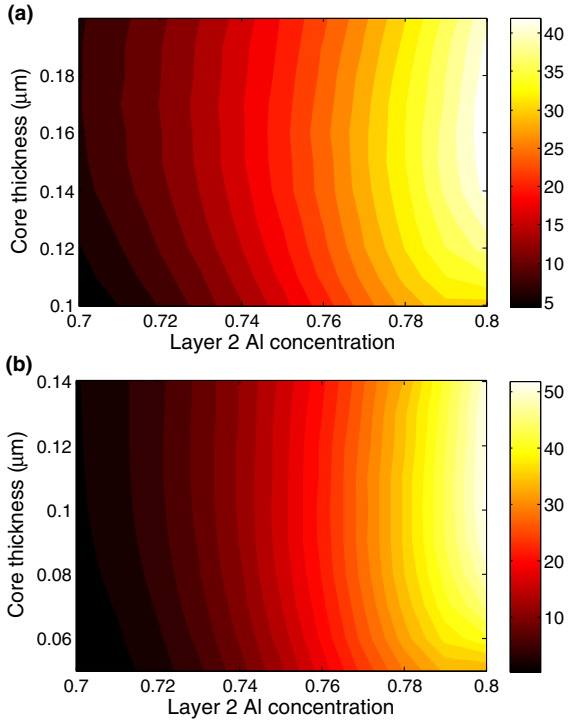

Fig. 8. Normalized nonlinear conversion efficiency in $\%\mathrm{W}^{-1}\,\mathrm{cm}^{-2}$ for (a) type-I and (b) type-II phase-matching as a function of core thickness and x_2. The structure parameters for type-I are $(x_1, x_m, x_c) = (0.3, 0.2, 0.85)$ with maximum η_{norm} at $(t_c, x_2) = (160\ \mathrm{nm}, 0.8)$ with a value of $0.41 \times 10^{-2}\,\%\ \mathrm{W}^{-1}\,\mathrm{cm}^{-2}$. The structure parameters for type-II are $(x_1, x_m, x_c) = (0.3, 0.2, 0.85)$ with maximum efficiency at $(t_c, x_2) = (140\ \mathrm{nm}, 0.8)$ with a value $0.515 \times 10^{-2}\,\%\ \mathrm{W}^{-1}\,\mathrm{cm}^{-2}$.

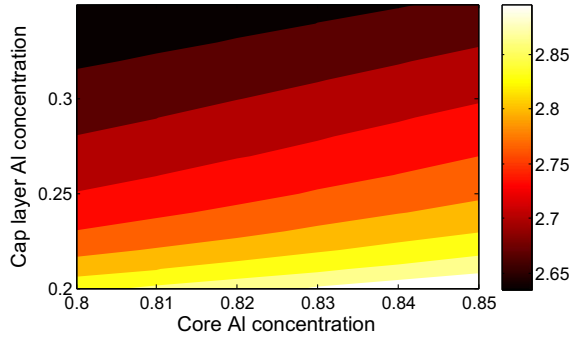

Fig. 9. GVM in ps/mm as a function of cap and core layer aluminum concentrations; structure parameters are $(x_1, x_2, t_c, t_m) = (0.4, 0.55, 310\ \mathrm{nm}, 286.9\ \mathrm{nm})$. Minimum GVM takes place at $(x_c, x_m) = (0.8, 0.35)$ and has a value of 2.6354 ps/mm.

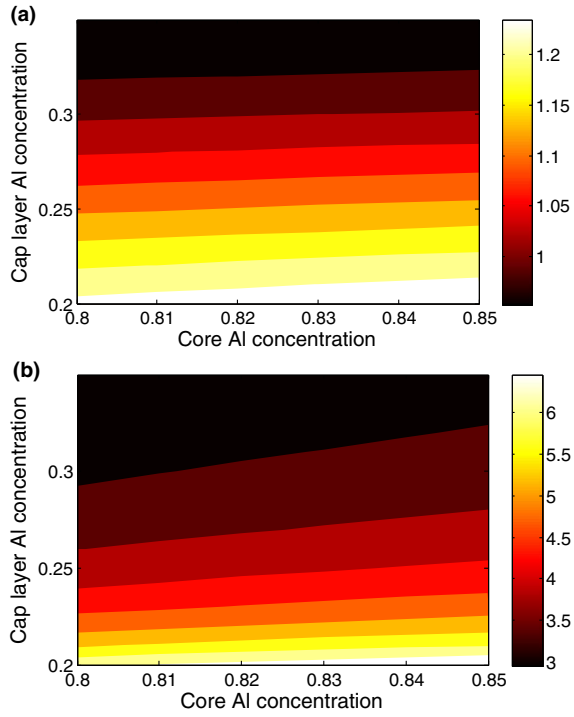

Fig. 10. GVD in $fs^2/\mu m$ of (a) pump and (b) second harmonic as a function of cap and core layer aluminum concentrations; structure parameters are $(x_1, x_2, t_c, t_m) = (0.4, 0.55, 310\ nm, 286.9\ nm)$. Minimum GVD is at $(x_c, x_m) = (0.8, 0.35)$ and has a value of 0.95258 $fs^2/\mu m$ for the pump and 2.9513 $fs^2/\mu m$ for the second harmonic.

Also, the GVM and GVD values are close to those obtained in ML-BRWs [24].

5. DEVICE STRUCTURE AND FABRICATION

The IMW wafer was grown, nominally undoped, using metal-organic chemical vapor deposition on a [001]-GaAs substrate. A buffer layer of $Al_{0.85}Ga_{0.15}As$ with a thickness of 500 nm was grown on top of the substrate. The structure was composed of a 140 nm thick core layer of $Al_{0.85}Ga_{0.15}As$ followed on each side by a 224.9 nm thick $Al_{0.20}Ga_{0.80}As$ cap layer. The top and bottom claddings consisted of six and seven periods, respectively, of alternating high and low Al concentration $Al_xGa_{1-x}As$. Each period contained a layer with a thickness of 127.4 nm $Al_{0.30}Ga_{0.70}As$ and a layer with a thickness of 463.3 nm thick $Al_{0.80}Ga_{0.20}As$. Ridge waveguides with widths varying between 2.65 and 4.65 μm were patterned using plasma etching.

The wafer was designed for type-II PM of SHG with a pump at 1540 nm and SH signal at 741 nm. Simulations verified that the same wafer could support type-I SHG with a pump at 1523.2 nm and a SH at 761.6 nm. Linear characterization of these devices is discussed first, after which the nonlinear is presented.

Table 1. Comparison of Nonlinear Interaction and Dispersion of QtW-BRW [18], ML-BRW [24], and IMW for Maximized η_{norm}

Design	η_{norm} [$\%W^{-1}\ cm^{-2}$]	GVM [ps/mm]	GVD_ω [fs^2/mm]	$GVD_{2\omega}$ [$fs^2/\mu m$]
QtW-BRW	0.638×10^{-4}	2.3674	763	1909
ML-BRW	2.150×10^{-4}	2.4058	1.4398	6.6349
IMW	0.410×10^{-4}	2.1483	1.3674	9.6646

Table 2. Comparison of Nonlinear Interaction and Dispersion of ML-BRW [24] and IMW for Maximized GVM

Design	η_{norm} [$\%W^{-1}\ cm^{-2}$]	GVM [ps/mm]	GVD_ω [fs^2/mm]	$GVD_{2\omega}$ [$fs^2/\mu m$]
ML-BRW	0.045×10^{-4}	1.7300	1.2616	2.8749
IMW	0.003×10^{-4}	2.6354	0.9526	2.9513

6. DEVICE CHARACTERIZATION

The devices linear properties were measured using the Fabry–Perot method [30]. A tunable distributed feedback laser source was tuned around the pump wavelength of 1550 nm, and device losses were extracted. The lowest loss values were recorded for a ridge width of about 2.76 μm with estimated loss values of 2.71 cm^{-1} and 4.26 cm^{-1} for TE and TM polarizations, respectively. The Fresnel reflection coefficient at the waveguide facets was estimated to be 26%. The input coupling factor defined as the spatial field overlap between the incident pump beam and the excited TIR pump mode was determined to be 18%. The length of the sample was ≈2.0 mm.

Table 4 provides a summary of the examined SHG parameters, including PM wavelength (λ_{PM}), FWHM pump spectral bandwidth ($\Delta\lambda_p$), internal pump power (P_ω), internal SH power ($P_{2\omega}$), SHG wavelength acceptance bandwidth ($\Delta\lambda_{SHG}$), normalized nonlinear conversion efficiency (η_{norm}), and the ratio $\Delta\lambda = \Delta\lambda_{SHG}/\Delta\lambda_\omega$.

The best performing waveguides were then characterized for SHG using three different laser systems, namely, (1) a programmable laser from Genia Photonics Inc. generating pulses with 30 ps temporal width ($\Delta\tau$) at 15 MHz repetition rate; (2) an OPO synchronously pumped by a mode-locked Ti:sapphire laser generating 2 ps pulses at 76 MHz repetition rate; and (3) a tunable single-mode continuous wave laser. The characterization was carried out in an end-fire coupling setup.

The tuning curve for all three sources is shown in Fig. 11. From the figures, for type-I and type-II processes, clear peaks in the SH power around ≈1534 nm and ≈1546 nm, respectively, are evident, indicating phase-matched processes at these wavelengths. The nature of the detected upconverted signal was confirmed by monitoring its power as a function of the pump power. The result is shown in Fig. 12 where the SH power versus pump power is plotted on a log–log scale. The solid line in the figure is a linear fit with an extracted slope of ≈2 confirming the quadratic relation between $P_{2\omega}$ and P_ω.

Table 3. Comparison of Nonlinear Interaction and Dispersion of ML-BRW [24] and IMW for Maximized $GVD_{2\omega}$

Design	η_{norm} [$\%W^{-1}\ cm^{-2}$]	GVM [ps/mm]	GVD_ω [fs^2/mm]	$GVD_{2\omega}$ [$fs^2/\mu m$]
ML-BRW	0.014×10^{-4}	1.9259	1.1704	2.2125
IMW	0.003×10^{-4}	2.6354	0.9526	2.9513

Table 4. Summary of SHG Characterization Using 2 ps, 30 ps, and Continuous Wave Pump Sources

Parameter	Type-I	Type-II	Type-I	Type-II	Type-I	Type-II
$\Delta\tau$ [ps]	2	2	30	30	CW	CW
$\Delta\lambda_p$ [nm]	3.1	3.1	0.3	0.3	–	–
P_ω [mW]	0.52	0.52	0.83	0.83	0.40	0.40
$P_{2\omega}$ [μW]	0.62	1.23	0.56	0.57	4.02×10^{-4}	4.14×10^{-4}
η_{norm} [%W^{-1} cm^{-2}]	5.73×10^3	1.14×10^4	2.03×10^3	2.07×10^3	6.28	6.47
$\Delta\lambda_{\text{SHG}}$ [nm]	1.7	1.8	0.9	0.8	0.7	0.7
$\Delta\lambda$	0.5	0.6	3.0	2.7	–	–

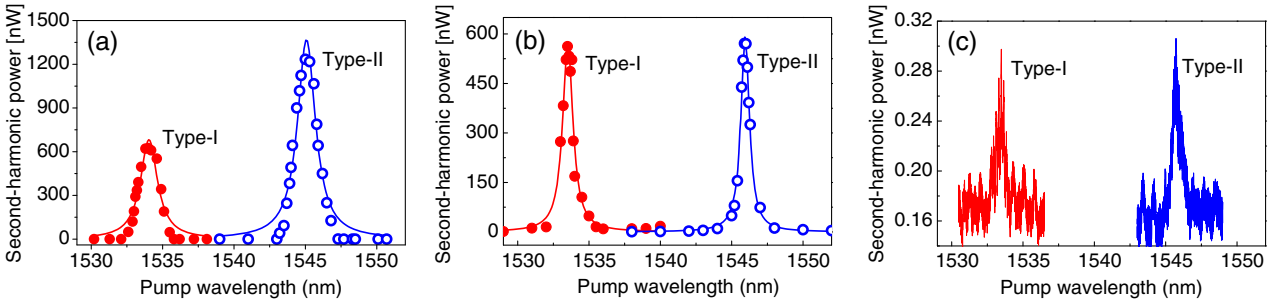

Fig. 11. Dependence of second-harmonic power on pump wavelength obtained using (a) 2 ps pulsed laser; (b) 30 ps pulsed laser; and (c) continuous wave laser for type-I and type-II phase matching.

The conversion efficiency is proportional to the peak powers obtained from the three sources. Efficiency is highest for the 2 ps source and lowest for the CW source. However, the ratio between the conversion efficiency values is smaller than the ratio of the peak powers. This difference in the ratios originates from nonlinear losses associated with two-photon absorption. The excess losses associated with two-photon absorption of the pump in the pulsed regime counteracts the increase in the peak power and clamps the conversion efficiency. Also, examining the difference in device performance using the 2 and 30 ps pulses is informative. From Table 4, it can be seen that changing the pulse width from 30 to 2 ps affected η_{norm} only by a factor of ≈2. Although the temporal pulse widths of 30 and 2 ps laser systems were different by over an order of magnitude, the duty cycles of the pulses were within the same orders of magnitude. For the 30 ps laser, the pulse duty cycle was 4.5×10^{-4} while it was 1.5×10^{-4} for the 2 ps laser. Assuming nearly transform-limited pulses, for comparable pump powers, the peak powers in 30 and 2 ps systems were within the same order of magnitude. Hence, the generated SH should be comparable.

Spectra of the pump and SH are shown in Fig. 13 using the 2 and 30 ps pulses. Comparison of the pump spectral bandwidth, $\Delta\lambda_\omega$, and the wavelength acceptance bandwidth, $\Delta\lambda_{\text{SHG}}$, measured for the three pump laser systems, can provide additional information about the device properties. We consider the ratio $\Delta\lambda = \Delta\lambda_{\text{SHG}}/\Delta\lambda_p$ as a figure of merit indicating the portion of the pump spectra utilized in the SHG process. Using Table 4, for 30 ps pulses, the entire pump spectrum is utilized. However, when using the 2 ps pulsed pump, almost half the pump spectral width was utilized. This observation additionally explains the fact that the efficiency of the device using a 2 ps pulsed pump was not significantly different in comparison to the 30 ps pulsed system.

The conversion efficiency values achieved using IMs in this work are an order of magnitude smaller in comparison to those achieved so far by BRWs [7]; hence, further optimization could improve the current design for phase-matching TIR and coupled IMs. Comparing the device here with other phase-matched structures in AlGaAs is also noteworthy. For example, in [31], frequency doubling of a continuous wave telecommunication pump has been reported where CW conversion efficiency of ≈14% W^{-1} cm^{-2} was obtained in a modal phase-matched AlGaAs nanowire. To the best of our knowledge, the higher conversion efficiency in this material system has been observed in artificial birefringence devices, where the extracted CW NL efficiency was as high as 1.12×10^3% W^{-1} cm^{-2} [32]. IMWs could also be utilized in conjunction with Bragg modes to offer further flexibility for some applications. The addition of a third, new type of mode supported in the same structure, where the Bragg and TIR modes exist, provides the opportunity to explore three-wave mixing processes other than second-harmonic generation; these include SFG and DFG, which could be achieved with better optimization of the three types of modes semi-independently. The modal overlap

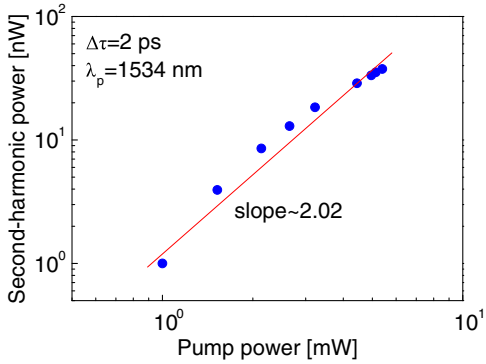

Fig. 12. Second-harmonic power as a function of pump power plotted on a log-log scale for type-II phase matching using 2 ps pulsed pump.

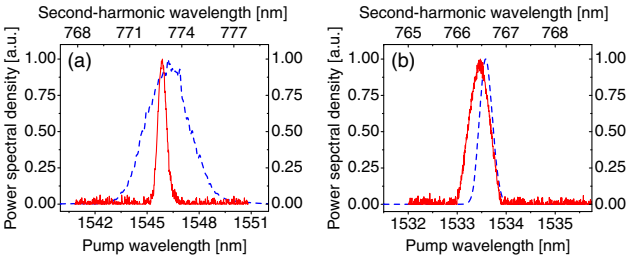

Fig. 13. Power spectral density of the pump (dashed line) and the corresponding second-harmonic (solid line) for type-II phase matching using (a) 2 ps pulsed pump and (b) 30 ps pulsed pump.

between Bragg modes and IMWs is better than that of the TIR mode with either the IMW or the Bragg mode. This improved modal overlap leads to greater nonlinear conversion efficiency for second-order nonlinear processes. Furthermore, the process bandwidth tunability, afforded by using IMWs to control the waveguide properties, is more accessible and versatile. This can be a key parameter in applications where the quantum optical properties of photons need to be engineered [12]. This platform can also play a key role in sensing applications [33].

7. CONCLUSION

We have proposed, theoretically analyzed, and experimentally demonstrated the behavior of IMWs for second-order nonlinear interactions. The waveguide structures in which these modes propagate have been fabricated, and linear and nonlinear properties of the modes have been examined. A conversion efficiency of $1.14 \times 10^4\%\ \mathrm{W}^{-1}\ \mathrm{cm}^{-2}$ has been achieved for type-II phase matching of a second-harmonic-generation process.

ACKNOWLEDGMENTS

We thank the Natural Sciences and Engineering Research Council of Canada (NSERC) for funding this research and CMC Microsystems for growing the wafers.

REFERENCES

1. A. Fiore, S. Janz, L. Delobel, P. van der Meer, P. Bravetti, V. Berger, and E. Rosencher, "Second-harmonic generation at λ = 1.6 μm in AlGaAs/Al_2O_3 waveguides using birefringence phase matching," Appl. Phys. Lett. **72**, 2942–2945 (1998).
2. R. Haidar, N. Forget, and E. Rosencher, "Optical parametric oscillation in micro-cavities based on isotropic semiconductors: a theoretical study," IEEE J. Quantum Electron. **39**, 569–576 (2003).
3. D. Artigas, E. U. Rafailov, P. Loza-Alvarez, and W. Sibbett, "Periodically switched nonlinear structures for frequency conversion: theory and experimental demonstration," IEEE J. Quantum Electron. **40**, 1122–1130 (2004).
4. K. L. Vodopyanov, O. Levi, P. S. Kuo, T. J. Pinguet, J. S. Harris, M. M. Fejer, B. Gerard, L. Becouarn, and E. Lallier, "Optical parametric oscillation in quasi-phase-matched GaAs," Opt. Lett. **29**, 1912–1914 (2004).
5. A. S. Helmy, "Phase matching using Bragg reflection waveguides for monolithic nonlinear optics applications," Opt. Express **14**, 1243–1252 (2006).
6. B. J. Bijlani and A. S. Helmy, "Bragg reflection waveguide diode lasers," Opt. Lett. **34**, 3734–3736 (2009).
7. P. Abolghasem, J. B. Han, B. J. Bijlani, A. Arjmand, and A. S. Helmy, "Highly efficient second-harmonic generation in monolithic matching layer enhanced $Al_xGa_{1-x}As$ Bragg reflection waveguides," IEEE Photon. Technol. Lett. **21**, 1462–1464 (2009).
8. J. B. Han, P. Abolghasem, B. J. Bijlani, and A. S. Helmy, "Continuous-wave sum-frequency generation in AlGaAs Bragg reflection waveguides," Opt. Lett. **34**, 3656–3658 (2009).
9. J. B. Han, P. Abolghasem, D. Kang, B. J. Bijlani, and A. S. Helmy, "Difference-frequency generation in AlGaAs Bragg reflection waveguides," Opt. Lett. **35**, 2334–2336 (2010).
10. R. T. Horn, P. Kolenderski, D. Kang, P. Abolghasem, C. Scarcella, A. D. Frera, A. Tosi, L. G. Helt, S. V. Zhukovsky, J. E. Sipe, G. Weihs, A. S. Helmy, and T. Jennewein, "Inherent polarization entanglement generated from a monolithic semiconductor chip," Sci. Rep. **3**, 2314 (2013).
11. B. J. Bijlani, P. Abolghasem, and A. S. Helmy, "Semiconductor optical parametric generators in isotropic semiconductor diode lasers," Appl. Phys. Lett. **103**, 091103 (2013).
12. P. Abolghasem, M. Hendrych, X. J. Shi, J. P. Torres, and A. S. Helmy, "Bandwidth control of paired photons generated in monolithic Bragg reflection waveguides," Opt. Lett. **34**, 2000–2002 (2009).
13. M. I. D'yakonov, "New type of electromagnetic wave propagating at an interface," Sov. Phys. JETP **67**, 714–716 (1988).
14. O. Takayama, L. Crasovan, D. Artigas, and L. Torner, "Observation of Dyakonov surface waves," Phys. Rev. Lett. **102**, 043903 (2009).
15. O. Takayama, L. C. Crasovan, S. K. Johansen, D. Mihalache, D. Artigas, and L. Torner, "Dyakonov surface waves: a review," Electromagnetics **28**, 126–145 (2008).
16. J. A. Polo and A. Lakhtakia, "Review of surface-wave propagation at the planar interface of a columnar or chiral sculptured thin film and an isotropic substrate," Nanostruct. Thin Films **7041**, E410 (2008).
17. P. Yeh, A. Yariv, and A. Y. Cho, "Optical surface waves in periodic layered media," Appl. Phys. Lett. **32**, 104–105 (1978).
18. B. R. West and A. S. Helmy, "Analysis and design equations for phase matching using Bragg reflection waveguides," IEEE J. Sel. Top. Quantum Electron. **12**, 431–442 (2006).
19. A. Arjmand, P. Abolghasem, J. Han, and A. S. Helmy, "Coupled interface modes for nonlinear interaction in periodic layered media," in *IEEE Lasers and Electro-Optics Society Annual Meeting* (IEEE, 2010) pp. 606–607.
20. C. Vandenbem, "Electromagnetic surface waves of multilayer stacks: coupling between guided modes and Bloch modes," Opt. Lett. **33**, 2260–2262 (2008).
21. A. Shinn and W. M. Robertson, "Surface plasmon-like sensor based on surface electromagnetic waves in a photonic bandgap material," Sens. Actuators B **105**, 360–364 (2005).
22. E. Guillermain, V. Lysenko, and T. Benyattou, "Surface wave photonic device based on porous silicon multilayers," J. Lumin. **121**, 319–321 (2006).
23. F. Villa, L. E. Regalado, F. Ramos-Mendieta, J. Gaspar-Armenta, and T. Lopez-Rios, "Photonic crystal sensor based on surface waves for thin-film characterization," Opt. Lett. **27**, 646–648 (2002).
24. P. Abolghasem and A. S. Helmy, "Matching layers in Bragg reflection waveguides for enhanced nonlinear interaction," IEEE J. Quantum Electron. **45**, 646–653 (2009).
25. V. Eckhouse, I. Cestier, G. Eisenstein, S. Combrie, P. Colman, A. De Rossi, M. Santagiustina, C. G. Someda, and G. Vadala, "Highly efficient four wave mixing in GaInP photonic crystal waveguides," Opt. Lett. **35**, 1440–1442 (2010).
26. A. Baron, A. Ryasnyanskiy, N. Dubreuil, P. Delaye, Q. V. Tran, S. Combrie, A. de Rossi, R. Frey, and G. Roosen, "Light localization induced enhancement of third order nonlinearities in a gas photonic crystal waveguide," Opt. Express **17**, 552–557 (2009).
27. J. Khurgin, "Improvement of frequency-conversion efficiency in waveguides with rotationally twinned layers," Opt. Lett. **13**, 603–605 (1988).
28. M. Ohashi, T. Kondo, R. Ito, S. Fukatsu, Y. Shiraki, K. Kumata, and S. S. Kano, "Determination of quadratic nonlinear optical coefficient of $Al_xGa_{1-x}As$ system by the method of reflected second harmonics," J. Appl. Phys. **74**, 596–601 (1993).
29. Y. Sakurai and F. Koyama, "Control of group delay and chromatic dispersion in tunable hollow waveguide with highly reflective mirrors," Jpn. J. Appl. Phys. **43**, 5828–5831 (2004).

30. T. Feuchter and C. Thristrup, "High-precision planar wave-guide propagation loss measurement technique using a Fabry–Perot cavity," IEEE Photon. Technol. Lett. **6**, 1244–1247 (1994).
31. D. Duchesne, K. A. Rutkowska, M. Volatier, F. Lgar, S. Delprat, M. Chaker, D. Modotto, A. Locatelli, C. De Angelis, M. Sorel, D. N. Christodoulides, G. Salamo, R. Ars, V. Aimez, and R. Morandotti, "Second harmonic generation in AlGaAs photonic wires using low power continuous wave light," Opt. Express **19**, 12408–12417 (2011).
32. M. Savanier, A. Andronico, A. Lematre, E. Galopin, C. Manquest, I. Favero, S. Ducci, and G. Leo, "Large second-harmonic generation at 1.55 m in oxidized AlGaAs waveguides," Opt. Lett. **36**, 2955–2957 (2011).
33. X. Zhang, A. Hosseini, H. Subbaraman, S. Wang, Q. Zhan, J. Luo, A. K.-Y. Jen, and R. T. Chen, "Integrated photonic electromagnetic field sensor based on broadband bowtie antenna coupled silicon organic hybrid modulator," J. Lightwave Technol. **32**, 3774–3784 (2014).